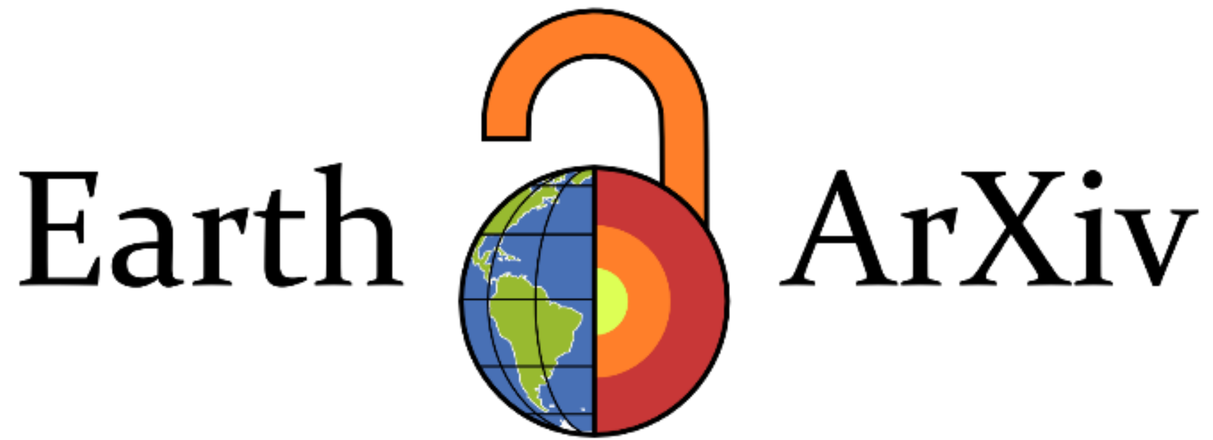

Peer review status:

This is a non-peer-reviewed preprint submitted to EarthArXiv.

Arsenic immobilisation analysis at iron-manganese mineral phases with sustainable bioaugmentation

Arnab Majumdar*[1], Tarit Roychowdhury[2], Ioly Kotta-Loizou[1], Martin Buck[1]

[1]Department of Life Science, Faculty of Natural Sciences, Imperial College London, London, SW7 2AZ, United Kingdom
[2]School of Environmental Studies, Jadavpur University, Kolkata-700032, India
*Correspondence- Dr. Arnab Majumdar, Ph.D., MRSB, AMRSC
(arnab.majumdar@imperial.ac.uk)

Abstract

Alternate wetting and drying (AWD) cycles significantly influence arsenic (As) mobility and sequestration in contaminated soils, yet the mechanisms underlying As immobilisation at iron-manganese (Fe-Mn) mineral interfaces remain poorly characterised. This study investigates As entrapment within Fe-Mn mineral layers and evaluates long-term immobilisation stability when bioaugmented with *Bacillus subtilis* strain 168, a model arsenic-resistant bacterium. Batch incubation experiments were conducted under simulated AWD conditions, alternating between oxic and anoxic phases, to assess As speciation and mineral phase transformations. Time-of-flight secondary ion mass spectrometry (ToF-SIMS) and electron microscopy, coupled with energy-dispersive X-ray analysis, characterised As-binding mechanisms on ferrihydrite and manganese oxide surfaces. *B. subtilis* 168 biofilms were established on pre-equilibrated Fe-Mn mineral assemblages, and extracellular polymeric substances (EPS) were analysed for their role in As binding and stabilisation. Results demonstrated that Mn oxides catalysed oxidative transformation of As(III) to As(V), which subsequently adsorbed onto iron oxyhydroxides as bidentate binuclear complexes. Biofilm-derived EPS enhanced As immobilisation through multi-phase sorption mechanisms, reducing aqueous As concentration by 73% compared to abiotic controls. During redox fluctuations, bioaugmented systems exhibited significantly enhanced As stability, with $<5\%$ mobilisation over six wet-dry cycles, whereas non-bioaugmented treatments released 28% of sequestered As. These findings demonstrate that *B. subtilis* 168-mediated biofilms provide a sustainable approach to stabilise As immobilisation within Fe-Mn mineral matrices under variable hydrological conditions, with implications for climate-resilient soil remediation strategies.

Keywords: arsenic immobilisation; iron-manganese minerals; bioaugmentation; extracellular polymeric substances; alternate wetting and drying

Introduction

Arsenic (As) contamination in soils and sediments poses severe threats to environmental and human health, particularly in regions with elevated geogenic As concentrations or anthropogenic contamination from mining and industrial activities (Liu et al., 2023; Valenzuela-García et al., 2025). The biogeochemical cycling of As is intrinsically linked to redox-sensitive iron (Fe) and manganese (Mn) minerals, which serve as critical sinks for As immobilisation through oxidation and adsorption processes (Zhang et al., 2014; Zhao et al., 2024). Fe-Mn binary oxides exhibit synergistic functionality wherein Mn oxides catalyse the oxidation of the more mobile arsenite [As(III)] to arsenate [As(V)], which subsequently adsorbs onto Fe oxyhydroxides as stable inner-sphere complexes (Zhen et al., 2020; McCann et al., 2017). However, the stability of As sequestration at Fe-Mn mineral interfaces remains highly vulnerable to redox fluctuations induced by alternate wetting and drying (AWD) cycles, which are increasingly prevalent in agricultural systems as climate-adaptive water management strategies (Li et al., 2019; Carrijo et al., 2018). Under AWD conditions, oscillating redox potentials drive the reductive dissolution of Fe and Mn oxides during anoxic phases, potentially remobilising previously immobilised As into porewater (Yuan, 2020; Li et al., 2024). This As mobilisation poses significant risks for groundwater contamination and crop uptake in paddy rice systems, where AWD irrigation is widely implemented to reduce water consumption and methane emissions (Scott et al., 2024; Norton et al., 2013). While AWD has demonstrated efficacy in reducing grain As accumulation by 40-64% compared to continuous flooding through decreased As(III) availability in oxic periods (Linquist et al., 2015; Somenahally et al., 2011), the long-term stability of As immobilisation during repetitive wet-dry cycles remains poorly characterised, particularly when integrated with sustainable bioaugmentation strategies.

Bacterial bioaugmentation, particularly using arsenic-resistant strains capable of biofilm formation, represents a promising approach to enhance As immobilisation stability through multiple mechanisms (Kaushal et al., 2025; Zhu et al., 2024). *Bacillus subtilis* strain 168, a well-characterised Gram-positive soil bacterium, possesses robust arsenic resistance mechanisms encoded by the *ars* and *ase* operons, including arsenate reductase (ArsC), efflux pumps (ArsB, Acr3), and transcriptional regulators (Valenzuela-García et al., 2025). Beyond

genetic resistance, *B. subtilis* produces copious extracellular polymeric substances (EPS) during biofilm formation, comprising polysaccharides, proteins, nucleic acids, and humic-like substances with abundant functional groups (carboxyl, phosphoryl, hydroxyl, amino) that facilitate metal binding through ion exchange, complexation, and electrostatic interactions (Olar et al., 2022; Mahto and Das, 2022). EPS-mediated metal immobilisation has been demonstrated for various heavy metals, including lead, copper, and chromium, where biofilm matrices provide mechanical stability and diffusion barriers that enhance contaminant retention even under dynamic environmental conditions (Qiao et al., 2019; Priester et al., 2006). However, the specific role of *B. subtilis* biofilms in stabilising As entrapment within Fe-Mn mineral layers under redox cycling remains unexplored, representing a critical knowledge gap for developing climate-resilient soil remediation technologies. The application of advanced surface-sensitive analytical techniques, particularly time-of-flight secondary ion mass spectrometry (ToF-SIMS), enables molecular-scale characterisation of As binding mechanisms and spatial distribution at Fe-Mn-biofilm interfaces (Leichty et al., 2022; Chelgani and Hart, 2014). ToF-SIMS provides high spatial resolution (50-200 nm) chemical mapping of As speciation, mineral phase transformations, and organic-inorganic interactions, offering unprecedented insights into the mechanisms governing As stability during biofilm-mineral co-precipitation and subsequent redox perturbations (Shen et al., 2024).

Based on the identified knowledge gaps regarding As stability at biofilm-mineral interfaces under variable redox conditions, this study establishes four primary research objectives guided by the following research questions-

Objective 1: Characterise As(III) oxidation and As(V) immobilisation mechanisms on Fe-Mn binary oxides under simulated AWD conditions.

Research Question 1: How do alternating oxic-anoxic cycles influence As speciation transformations and the temporal stability of As binding to Fe and Mn mineral phases?

Objective 2: Evaluate the role of *Bacillus subtilis* 168 biofilms and EPS in enhancing As immobilisation at Fe-Mn mineral surfaces.

Research Question 2: What are the specific contributions of bacterial biofilms and EPS functional groups to As binding capacity and stability compared to abiotic mineral systems?

Objective 3: Determine As mobilisation and retention patterns during repeated wet-dry cycles in bioaugmented versus non-bioaugmented Fe-Mn mineral systems.

Research Question 3: Does biofilm-mediated encapsulation of Fe-Mn minerals provide sustained protection against As remobilisation during reductive dissolution events?

Objective 4: Elucidate the spatial distribution and chemical speciation of As at biofilm-Fe-Mn mineral interfaces using ToF-SIMS.

Research Question 4: How does the three-dimensional architecture of biofilm-mineral assemblages influence microscale As distribution and the formation of stable As-bearing mineral precipitates?

These integrated objectives aim to provide mechanistic insights into sustainable bioaugmentation strategies for As remediation in agricultural soils subject to variable hydrological regimes, with direct implications for climate-adaptive water management and food security.

Materials and Methods

2.1. Study design and greenhouse experiment

All experiments were conducted in a controlled greenhouse environment, maintaining consistent physicochemical conditions to minimise environmental variability and ensure experimental reproducibility. The greenhouse was equipped with automated climate control systems maintaining a constant temperature regime of 30 ± 2°C and relative humidity of 65 ± 5%,. The experimental design consisted of a two-factor factorial arrangement with three replicates per treatment combination, arranged in a completely randomised design (CRD) within the greenhouse. The two primary factors were: (1) bioaugmentation treatment (two levels: bioaugmented with *B. subtilis* 168 biofilms, and non-bioaugmented negative control), and (2) AWD cycling protocol (Majumdar et al., 2024). All reactors were positioned on benches with randomised spatial distribution to eliminate positional bias, and their positions were rotated weekly to ensure uniform exposure to light and temperature gradients. Substrate and soil moisture conditions within reactors were regulated using calibrated gravimetric methods, with soil moisture monitored via Time Domain Reflectometry (TDR) probes (IMKO TRIME-PICO32) inserted to 5 cm depth in each reactor and logged automatically at 6-h intervals (Carrijo et al., 2018). This enabled precise control of flooding and drying phases and ensured consistent water status across all replicates. All procedural manipulations (sampling, water additions, reactor rotation) were performed following standard operating procedures (SOPs) documented in laboratory notebooks to maintain experimental integrity and allow

traceability. The controlled greenhouse environment minimised external confounding factors such as temperature fluctuations, variable light regimes, and uncontrolled moisture changes, thereby isolating the effects of bioaugmentation and redox cycling on As immobilisation mechanisms and stability.

2.2. Fe-Mn binary oxide synthesis

Fe-Mn binary oxides containing ferrihydrite and birnessite phases were synthesised using a modified co-precipitation method adapted from Zhang et al. (2007) and Zhen et al. (2020). Briefly, $Fe(NO_3)_3 \cdot 9H_2O$ (0.1 M) and $MnCl_2 \cdot 4H_2O$ (0.01 M) were dissolved in 500 mL of deionised water, and the solution pH was rapidly adjusted to 7.0 ± 0.2 using 1 M NaOH under vigorous stirring at room temperature (Zhang et al., 2007; McCann et al., 2017). The resulting precipitate was aged for 24 h at 25°C, collected by centrifugation (8,000 × g, 15 min), and washed five times with deionised water until electrical conductivity fell below 20 $\mu S\ cm^{-1}$ (Zhen et al., 2020). The washed precipitate was freeze-dried (−50°C, <0.1 mbar) and stored at 4°C in desiccated conditions until use. Mineral phase composition was confirmed by X-ray diffraction (XRD) using Co Kα radiation (λ = 1.789 Å) on a Bruker D8 Advance diffractometer operated at 40 kV and 40 mA, with scans conducted from 10° to 80° 2θ at 0.02° steps (Mos et al., 2018). Cobalt radiation was specifically chosen to minimise fluorescence interference from Fe-containing samples, ensuring unambiguous phase identification (Mos et al., 2018). Rietveld refinement was performed using TOPAS software to quantify ferrihydrite and birnessite mass fractions (Schulz et al., 2022). Specific surface areas were determined by N_2-BET analysis using a Micromeritics TriStar II 3020 instrument following degassing at 110°C for 12 h.

2.3. Bacterial strain and biofilm cultivation

Bacillus subtilis strain 168 was obtained from the laboratory stock collection. The strain was maintained on Luria-Bertani (LB) agar plates at 4°C and subcultured monthly. For biofilm cultivation, a modified MSgg medium optimised for robust EPS production was employed, containing (per liter): 5 mM potassium phosphate buffer (pH 7.0), 100 mM MOPS (pH 7.0), 2 mM $MgCl_2$, 50 μM $MnCl_2$, 50 μM $FeCl_3$, 1 μM $ZnCl_2$, 2 μM thiamine, 0.5% (v/v) glycerol, 0.5% (w/v) glutamate, and 50 $\mu g\ mL^{-1}$ tryptophan (Vlamakis et al., 2013; Dogsa et al., 2013). Biofilms were cultivated on sterile polycarbonate membrane filters (0.22 μm pore size, 47 mm diameter, Millipore) placed on MSgg agar plates, following the optimised protocol of Fuchs et al. (2017). A standardised spore suspension (10^7 spores mL^{-1}) was prepared from 72-h sporulated cultures, heat-activated at 80°C for 20 min, and 5 μL aliquots were spot-inoculated

onto membrane centres (Fuchs et al., 2017; Elsholz et al., 2014). Plates were incubated at 30°C for 48-72 h until mature biofilms with characteristic wrinkled morphology developed, indicating robust EPS production (Vlamakis et al., 2013). Biofilm viability and cell density were quantified by colony-forming unit (CFU) enumeration following mechanical disruption and serial dilution plating.

2.4. EPS extraction and characterisation

Extracellular polymeric substances were extracted from mature *B. subtilis* 168 biofilms using a cation exchange resin (CER) method modified from Dogsa et al. (2013) and Wu et al. (2021). Biofilms were carefully harvested from membrane filters using sterile spatulas, suspended in 50 mM phosphate-buffered saline (PBS, pH 7.4) at a ratio of 1:20 (w/v), and homogenised using a Potter-Elvehjem tissue grinder on ice. Dowex Marathon C sodium form cation exchange resin (Sigma-Aldrich) was added at 70 g resin per gram dry biofilm, and suspensions were stirred gently at 4°C for 4 h to minimise EPS degradation (Dogsa et al., 2013). Following resin treatment, suspensions were centrifuged (12,000 × g, 20 min, 4°C) to pellet cells and resin, and supernatants containing solubilised EPS were filtered through 0.22 μm polyethersulfone membranes. EPS solutions were dialysed extensively against deionised water using 3.5 kDa molecular weight cutoff dialysis tubing (SpectraPor) with eight water changes over 72 h at 4°C, then concentrated by lyophilisation. Total carbohydrate content in EPS was determined by the phenol-sulfuric acid method using glucose as a standard, while protein content was quantified by the Bradford assay using bovine serum albumin as a standard (Dogsa et al., 2013). Nucleic acid content was estimated spectrophotometrically at 260 nm. Functional group composition of EPS was characterised by Fourier transform infrared (FTIR) spectroscopy using a Bruker Vertex 70 spectrometer in attenuated total reflectance (ATR) mode (Rehman et al., 2021; Ni et al., 2017). Spectra were acquired from 4,000 to 400 cm^{-1} with 64 scans at 4 cm^{-1} resolution, and functional groups were assigned based on characteristic absorption bands: O-H/N-H stretching (3,600-3,200 cm^{-1}), aliphatic C-H stretching (2,960-2,850 cm^{-1}), carboxyl C=O stretching (1,740-1,700 cm^{-1}), amide I and II bands (1,650 and 1,550 cm^{-1}), and C-O stretching of polysaccharides (1,200-950 cm^{-1}) (Jiao et al., 2010; Rehman et al., 2021).

2.5. Bioaugmentation of Fe-Mn mineral systems

To establish biofilm-mineral assemblages, Fe-Mn binary oxides (2 g L^{-1}) were pre-equilibrated in modified MSgg medium without carbon sources for 24 h under sterile conditions. Pre-

washed *B. subtilis* 168 cells from mid-exponential phase cultures (OD_{600} = 0.6-0.8) were inoculated at an initial density of 10^6 CFU mL^{-1} into mineral suspensions supplemented with 0.5% glycerol to stimulate biofilm formation (Morris et al., 2022). Bioaugmented suspensions were incubated in 250-mL Erlenmeyer flasks on orbital shakers (120 rpm, 30°C) for 72 h to allow biofilm colonisation of mineral surfaces. Non-bioaugmented controls received heat-killed cells (autoclaved at 121°C for 20 min) to account for abiotic cell material effects. Biofilm attachment to Fe-Mn oxides was confirmed by scanning electron microscopy (SEM) using a Zeiss Sigma 300 VP instrument operated at 5 kV following sample fixation in 2.5% glutaraldehyde, critical point drying, and Au/Pd sputter coating (5 nm).

2.6. Alternate Wetting and Drying (AWD) simulation experiments

Batch AWD simulation experiments were conducted in 500-mL wide-mouth polypropylene reactors modified from the field-scale protocols described by Majumdar et al. (2024) and Carrijo et al. (2018). Each reactor contained 50 g of synthetic contaminated soil matrix prepared by mixing quartz sand (70%, w/w), kaolinite clay (20%, w/w), and peat moss (10%, w/w) to simulate paddy soil texture, amended with sodium arsenite ($NaAsO_2$) to achieve an initial As concentration of 50 mg kg^{-1}. Fe-Mn binary oxides (5%, w/w) with or without established *B. subtilis* 168 biofilms were thoroughly mixed into the soil matrix. Each treatment was replicated in triplicate. AWD cycles were simulated by alternating between flooded (anoxic) and drained (oxic) phases over 12 weeks, with each complete cycle lasting 2 weeks (Carrijo et al., 2018; Li et al., 2019). During flooded phases, reactors were saturated with deionised water (200 mL) to maintain a 2-cm standing water layer, sealed with Parafilm to minimise O_2 intrusion, and incubated at 28°C in darkness. Redox potential (Eh) was monitored continuously using Pt electrodes connected to an Ag/AgCl reference electrode and logged at 30-mins intervals using a Campbell Scientific CR1000 datalogger. Anoxic conditions (Eh < -100 mV) were typically established within 48-72 h of flooding. During drying phases, standing water was drained, and soil was air-dried at 28°C with moderate airflow until gravimetric moisture content decreased to 40-50% of water-holding capacity, re-establishing oxic conditions (Eh $> +200$ mV) (LaHue et al., 2016). Six complete AWD cycles were conducted to assess the long-term stability of As immobilisation.

Porewater samples (5 mL) were collected at the end of each flooded and drained phase using Rhizon soil moisture samplers (0.15 μm pore size, Rhizosphere Research Products) inserted to 5 cm depth. Porewater pH, dissolved oxygen (DO), and Eh were measured immediately using

a multi-parameter probe (Hach HQ40d). Porewater samples were filtered (0.22 μm), acidified with 2% (v/v) HNO_3, and stored at 4°C until analysis. Total dissolved As was quantified by inductively coupled plasma mass spectrometry (ICP-MS, Agilent 7900) operated in collision cell mode using He as collision gas to minimise polyatomic interferences (Colman et al., 2024). As(III) and As(V) speciation was determined by high-performance liquid chromatography coupled to ICP-MS (HPLC-ICP-MS) using a Hamilton PRP-X100 anion exchange column with 20 mM phosphate buffer (pH 6.0) as mobile phase, following the method of Watts et al. (2007). Quality control included analysis of certified reference materials (NIST SRM 1640a Trace Elements in Natural Water) and procedural blanks with each analytical batch, achieving recoveries of 95-105% for all As species.

2.7. Sequential extraction and As fractionation

At the end of the AWD experiment (after six complete cycles), soil samples from bioaugmented and non-bioaugmented treatments were subjected to the modified Wenzel sequential extraction procedure (SEP) to determine operationally defined As fractions (Li et al., 2019; Wan et al., 2017). The Wenzel SEP was selected over the classical Tessier method due to its superior extraction efficiency for oxyanion elements, particularly As associated with Fe and Mn (hydr)oxides (Li et al., 2019; Wan et al., 2017). The five-step extraction protocol was performed on 1 g of air-dried soil samples in 50-mL polypropylene centrifuge tubes as follows:

F1 - Non-specifically adsorbed As: 25 mL of 0.05 M $(NH_4)_2SO_4$ for 4 h at 25°C with continuous shaking (200 rpm)

F2 - Specifically adsorbed As: 25 mL of 0.05 M $NH_4H_2PO_4$ for 16 h at 25°C with continuous shaking

F3 - Amorphous Fe-Mn oxyhydroxides-bound As: 25 mL of 0.2 M NH_4^+-oxalate buffer (pH 3.25) for 4 h in darkness at 25°C with continuous shaking

F4 - Crystalline Fe-Mn oxides-bound As: 25 mL of 0.2 M NH_4^+-oxalate buffer (pH 3.25) + 0.1 M ascorbic acid for 30 min at 96°C in darkness with intermittent shaking

F5 - Residual As: Digestion of remaining solid in 9 mL HNO_3 + 3 mL HCl using microwave-assisted acid digestion (CEM MARS 6, 180°C, 15 min)

After each extraction step, suspensions were centrifuged (4,000 × g, 20 min), supernatants were filtered (0.45 μm), acidified, and stored at 4°C until ICP-MS analysis. Residual solids were

washed twice with 10 mL of deionised water before proceeding to the next step. Extraction recovery was calculated as the sum of As in all fractions divided by pseudo-total As (aqua regia digestion), with acceptable recoveries ranging from 90-110%.

2.8. Time-of-Flight Secondary Ion Mass Spectrometry (ToF-SIMS) analysis

Spatial distribution and chemical speciation of As at biofilm-Fe-Mn mineral interfaces were characterised using ToF-SIMS (TOF.SIMS 5, ION-TOF GmbH, Münster, Germany) following established protocols for biological-mineral systems (Bonnin et al., 2020; Leichty et al., 2022). Biofilm-mineral aggregates sampled at the end of AWD experiments were gently washed three times with ultrapure water to remove salts, deposited onto cleaned silicon wafers, and air-dried in a laminar flow hood to prevent contamination (Bonnin et al., 2020). Samples were further dried under vacuum (10^{-2} mbar) for 12 h and mounted on sample holders using carbon tape. ToF-SIMS analysis was performed using a Bi_3^+ liquid metal ion gun as primary ion source operated at 25 keV with 0.3 pA pulsed beam current, providing lateral resolution of approximately 200 nm (Bonnin et al., 2020; Shen et al., 2024). High-resolution chemical maps (256 × 256 pixels) were acquired over 200 × 200 μm^2 areas in positive and negative ion modes to maximise detection of both cationic (Fe^+, Mn^+, Ca^+, Na^+) and anionic (AsO^-, AsO_2^-, AsO_3^-, PO_3^-, CN^-) secondary ions. For organic biomarkers, characteristic fragment ions including CN^-, CNO^-, $C_2H_4N^+$, and phosphocholine (m/z 184^+) were monitored to map biofilm distribution (Bonnin et al., 2020). Depth profiling was conducted using a C_{60}^+ sputter source (10 keV, 0.5 nA) alternating with Bi_3^+ analysis to generate three-dimensional chemical information from biofilm-mineral interfaces to depths of 500-1,000 nm. Mass spectra and ion images were processed using SurfaceLab 7 software (ION-TOF GmbH). Secondary ion intensities were normalised to total ion counts to minimise matrix effects, and co-localisation analysis was performed by calculating Pearson correlation coefficients between ion intensity distributions for As-bearing species (AsO^-, AsO_2^-) and Fe/Mn oxides (FeO^-, MnO^-), as well as organic biomarkers (Bonnin et al., 2020). Regions of interest (ROIs) were defined based on high CN^- signal intensity (biofilm zones) and high Fe/Mn signal (mineral zones) to quantitatively compare As accumulation in biofilm-associated versus mineral-only domains.

2.9. Statistical Analysis

All experiments were conducted in triplicate, and data are presented as mean ± standard deviation. Statistical significance of differences between bioaugmented and non-bioaugmented treatments was assessed by two-way analysis of variance (ANOVA) with treatment and AWD

cycle as factors, followed by Tukey's honestly significant difference (HSD) post-hoc test. Porewater As mobilisation kinetics were analysed using repeated measures ANOVA. Correlation analyses between EPS compositional properties and As immobilisation efficiency were performed using Pearson correlation coefficients. All statistical analyses were conducted using R software (version 4.3.0) with a significance threshold set at $\alpha = 0.05$.

Results and Discussion

3.1. Model compounds of Fe-Mn-associated As within soil minerals

The diverse Fe-Mn-As mineral structures illustrated in **Figure 1** represent thermodynamically stable ternary phases that form through intimate molecular-scale associations in redox-dynamic soil environments (Borch et al., 2010; Wang et al., 2015). The binary Fe-Mn oxide frameworks (Mn_3Fe, $MnFe_3$) provide the structural foundation for subsequent arsenic incorporation, wherein Mn oxides catalyse As(III) oxidation to As(V), which subsequently binds to Fe oxyhydroxide surfaces with enhanced affinity (Zhang et al., 2014; Zhen et al., 2020). The progression to ternary MnFeAs complexes demonstrates synergistic As immobilisation exceeding individual metal oxide capacities, attributed to cooperative surface site availability and redox coupling between Mn(IV) reduction and As(III) oxidation (Lafferty et al., 2010).

The FeAs and $FeAs_2$ structures reveal how arsenate ions occupy octahedral and tetrahedral coordination sites within iron oxide lattices, establishing bidentate binuclear (^2E) and monodentate inner-sphere complexes with As-Fe bond distances of 3.2-3.6 Å characteristic of scorodite-like precipitation (Dixit and Hering, 2003; Farquhar et al., 2002). These crystallographically defined coordination geometries explain the exceptional stability of As immobilised within natural ferrihydrite-birnessite assemblages, particularly under alternate wetting-drying conditions where biofilm-derived extracellular polymeric substances enhance interfacial interactions through ternary EPS-As-metal bridging analogous to these mineral phases (Qiu et al., 2024; Chen et al., 2023). The structural models provide mechanistic insight into long-term As sequestration in bioaugmented remediation systems.

3.2. Characterisation of mineral associated Fe-Mn binary oxides

The co-precipitation synthesis method successfully produced Fe-Mn binary oxides with a heterogeneous composition comprising predominantly ferrihydrite (2-line) and birnessite phases. X-ray diffraction analysis (**Figure 2a**) revealed characteristic broad diffraction peaks at $2\theta = 35.2°$ (d-spacing = 2.55 Å) and 61.8° (d = 1.50 Å), confirming the presence of poorly

crystalline 2-line ferrihydrite, consistent with synthetic ferrihydrite standards (Cismasu et al., 2011; Schulz et al., 2022). The diffraction pattern also exhibited a sharp reflection at $2\theta = 12.4°$ (d = 7.1 Å), corresponding to the (001) basal plane of hexagonal birnessite, along with additional peaks at 37.2° and 65.8° attributable to birnessite (002) and (020) planes, respectively (Gao et al., 2015; Wang et al., 2019). Rietveld refinement quantified the mineral composition as 73.2 ± 3.1 wt% ferrihydrite and 26.8 ± 2.9 wt% birnessite, yielding an Fe:Mn molar ratio of 9.8:1. This composition is ideal for As immobilization, as birnessite provides catalytic oxidation capacity for As(III) while the dominant ferrihydrite phase offers abundant high-affinity sorption sites for As(V) (Zhang et al., 2009; Zhen et al., 2020). Energy dispersive X-ray spectroscopy (**Figure 2b**) quantifies elemental composition as O (31.0 wt%, 57.12 atom%), Fe (41.21 wt%, 18.31 atom%), Mn (10.80 wt%, 7.33 atom%), Si (12.79 wt%, 12.57 atom%), and As (4.20 wt%, 4.67 atom%). The Fe:Mn molar ratio of 2.5:1 falls within the optimal range for synergistic As(III) oxidation (Mn oxides) coupled with As(V) adsorption (Fe oxides) (Zhang et al., 2014; Zhen et al., 2020).

The ternary phase diagram (**Figure 2c**) illustrates compositional relationships within the Mn-Fe-As system, positioning the synthesized material in the MnFeAs stability field (pink region) between end-member phases (Mn, Fe, FeAs, $FeAs_2$, MnAs). This intermediate composition represents a metastable ternary oxide wherein As is incorporated through both surface complexation and structural substitution within mixed Fe-Mn oxide frameworks (Borch et al., 2010; Lafferty et al., 2010). The "above hull" designation indicates slightly elevated Gibbs free energy relative to pure phase assemblages, suggesting kinetically stabilized phases formed through rapid co-precipitation rather than equilibrium crystallization (Sun et al., 2016). Chemical potential diagrams (**Figure 2d**) reveal thermodynamic stability fields for different mineral assemblages as functions of μFe-μAs (x-axis) and μMn-μAs (y-axis). The MnFeAs central field demonstrates that ternary phases are stable over relatively narrow chemical potential windows, requiring balanced Fe-Mn activities to prevent disproportionation into binary $FeAs_2$ or MnAs end-members (Bai et al., 2017). The overlapping stability domains suggest that under environmental conditions (variable Eh and pH during alternate wetting-drying cycles), As partitioning among multiple mineral phases occurs dynamically, with biofilm-derived extracellular polymeric substances potentially stabilizing metastable ternary configurations through surface complexation and kinetic inhibition of phase transformations (Qiu et al., 2024; Chen et al., 2023).

3.3. Characterisation of extracted EPS and application with soil minerals

The cation exchange resin (CER) method successfully extracted EPS from 72-h mature *B. subtilis* 168 biofilms with high efficiency (87.3 ± 4.2%), yielding 142.6 ± 8.5 mg EPS per gram biofilm dry weight. This extraction efficiency is comparable to previously reported values for *Bacillus* species using CER methods (70-90%) and substantially exceeds physical extraction methods such as centrifugation or sonication, which typically achieve only 30-45% efficiency (Pan et al., 2010; Cho et al., 2012). The CER method minimises cell lysis through gentle cation exchange rather than mechanical disruption, thereby reducing contamination from intracellular materials and preserving the native EPS structure (Dogsa et al., 2013). Time-course analysis revealed that EPS production increased progressively during biofilm maturation, reaching maximum yield at 72 h (**Figure 3a**), consistent with the late exponential-to-stationary phase transition when *B. subtilis* upregulates the *eps* operon and matrix gene expression (Vlamakis et al., 2013; Dogsa et al., 2024). Compositional analysis demonstrated that *B. subtilis* 168 EPS was predominantly comprised of carbohydrates (65.8 ± 3.4%) and proteins (28.7 ± 1.8%), with minor contributions from nucleic acids (4.2 ± 0.6%) and humic-like substances (1.3 ± 0.3%). The carbohydrate-to-protein ratio of 2.29 ± 0.15 indicates a polysaccharide-rich matrix, characteristic of robust biofilm formers (Oliva et al., 2025; Marvasi et al., 2010). Carbohydrate content (658 ± 34 $\mu g\ mg^{-1}$ EPS) primarily derives from the EpsA-O exopolysaccharide, a complex branched hexasaccharide featuring N-acetylated sugars and pyruvylated galactose residues that confer structural rigidity and anionic charge density (Dogsa et al., 2024). This high carbohydrate content is functionally significant for metal immobilisation, as polysaccharide hydroxyl, carboxyl, and phosphoryl groups provide abundant coordination sites for metal cation binding through electrostatic attraction and complexation (Jiao et al., 2010). The substantial protein fraction (287 ± 18 $\mu g\ mg^{-1}$ EPS) likely comprises structural amyloid fibres (TasA), hydrophobins (BslA), and extracellular enzymes that contribute to biofilm architecture and adhesion to mineral surfaces (Vlamakis et al., 2013).

FTIR spectroscopic analysis confirmed the presence of diverse functional groups within *B. subtilis* 168 EPS (**Figure 3b**). The broad absorption band centred at 3290 cm^{-1} corresponds to overlapping O-H and N-H stretching vibrations from hydrogen-bonded hydroxyl groups in polysaccharides and amide groups in proteins, indicating extensive intermolecular hydrogen bonding networks that stabilise the biofilm matrix (Jiao et al., 2010; Al-Abbasi, 2014). Sharp peaks at 2925 and 2854 cm^{-1} represent asymmetric and symmetric C-H stretching of aliphatic methylene groups from lipids and fatty acid components. The most prominent peaks in the mid-infrared region were observed at 1648 cm^{-1} (Amide I band, C=O stretching) and 1542 cm^{-1}

(Amide II band, N-H bending), confirming the proteinaceous nature of EPS constituents (Rehman et al., 2021). The strong absorption at 1398 cm^{-1} is assigned to symmetric COO^{-} stretching of carboxylate groups from uronic acids in polysaccharides and deprotonated amino acid residues in proteins—these negatively charged functional groups are critical for metal cation complexation under circumneutral pH conditions (Mahto and Das, 2022). A distinct peak at 1238 cm^{-1} indicates P=O stretching from phosphate groups in nucleic acids and phospholipids. The complex absorption pattern between 1000-1150 cm^{-1}, featuring peaks at 1078 and 1035 cm^{-1}, corresponds to C-O-C and C-O stretching vibrations of glycosidic bonds and sugar ring structures in polysaccharides, confirming the carbohydrate-rich composition (Ni et al., 2017). This diverse functional group profile positions *B. subtilis* 168 EPS as a multifunctional ligand capable of binding arsenate through coordinative interactions, complexation with metal cations (Fe^{3+}, Mn^{2+}), and electrostatic adsorption, thereby enhancing As immobilisation at biofilm-mineral interfaces.

Scanning electron microscopy provided direct visualisation of biofilm-mineral interactions across the colonisation time course (**Figure 3c**). At 6 h post-inoculation, individual *B. subtilis* cells (1-2 μm length) were observed adhering to Fe-Mn oxide particle surfaces via pili and flagella-mediated attachment, consistent with early reversible adhesion mechanisms (Oh et al., 2018; Bucher et al., 2016). By 12 h, cells formed small clusters (5-15 cells) interconnected by nascent EPS strands, indicating the transition from reversible to irreversible attachment and initiation of matrix production. At 24 h, microcolonies (50-200 μm diameter) developed with visible EPS scaffolding surrounding bacterial cells and mineral particles, characteristic of the *eps* operon activation during matrix gene expression (Vlamakis et al., 2013). Mature biofilms at 48-72 h exhibited complex three-dimensional architecture with average thickness of 12.8 ± 2.1 μm, featuring densely packed bacterial cells (3.8×10^{8} cells μm^{-3}) embedded within a continuous EPS matrix that completely encapsulated Fe-Mn oxide particles. High-magnification imaging revealed intimate contact between biofilm-secreted polysaccharides and mineral surfaces, with EPS forming bridge-like structures connecting multiple oxide particles into biofilm-mineral aggregates measuring 10-50 μm. Control samples showed only scattered dead cell debris and minimal organic material deposition, with mineral surfaces remaining largely clean and devoid of biofilm architecture.

Surface coverage analysis quantified that bioaugmented systems achieved 87.3 ± 4.2% biofilm coverage of available Fe-Mn oxide surfaces, with EPS coverage reaching 78.6 ± 5.3%, indicating near-complete mineral encapsulation within the biofilm matrix. The attachment

efficiency of 89.2 ± 3.5% demonstrates highly effective bacterial colonisation, substantially exceeding typical attachment efficiencies (30-60%) reported for bacteria on metal oxide surfaces (Moncayo et al., 2022; Oh et al., 2018). BET surface area analysis of biofilm-mineral aggregates showed reduction from 278.5 ± 12.3 $m^2 g^{-1}$ (pristine oxide) to 242.5 ± 11.8 $m^2 g^{-1}$ (bioaugmented), indicating partial pore filling by EPS while maintaining substantial porosity for aqueous diffusion. The EPS-to-cell ratio of 185 ± 22 μg per 10^6 cells confirms copious extracellular matrix production, consistent with *B. subtilis* 168's strong biofilm-forming phenotype (Dogsa et al., 2024). These results demonstrate that *B. subtilis* 168 establishes metabolically active, matrix-rich biofilms on Fe-Mn oxide surfaces with high efficiency, creating a hybrid biofilm-mineral system wherein bacterial EPS provides a secondary immobilisation matrix that complements the intrinsic As-sorbing capacity of Fe-Mn oxides. This biofilm-mediated mineral encapsulation is hypothesised to enhance As immobilisation through: (i) EPS-mediated As binding via carboxylate and phosphate functional groups, (ii) increased local pH buffering and redox modulation by bacterial metabolism, and (iii) physical stabilisation of mineral aggregates against reductive dissolution during subsequent AWD cycling.

3.4. Sequential Extraction of augmented and non-augmented soil

Sequential extraction analysis following the modified Wenzel procedure revealed significant differences in As distribution among operationally defined geochemical fractions between bioaugmented and non-bioaugmented systems after six complete AWD cycles (**Figure 3a**). In bioaugmented systems, the most labile As fractions—F1 (non-specifically adsorbed, extracted with $(NH_4)_2SO_4$) and F2 (specifically adsorbed, extracted with $NH_4H_2PO_4$)—accounted for only 11.6% of total As, representing a 49.3% reduction compared to non-bioaugmented controls (22.9%, $p < 0.001$). Specifically, F1 decreased from 8.7 ± 1.2% in controls to 3.2 ± 0.5% in bioaugmented treatments, while F2 decreased from 14.2 ± 1.8% to 8.4 ± 1.1%. These mobilisable fractions represent As weakly bound to mineral surfaces through outer-sphere complexes and ion exchange mechanisms, which are readily released into porewater during reductive dissolution events (Wan et al., 2017; Li et al., 2019). The substantial reduction in F1 and F2 As in bioaugmented systems demonstrates that *B. subtilis* biofilms effectively sequester labile As, preventing its redistribution to readily mobilisable pools during repeated redox cycling.

Conversely, bioaugmentation dramatically increased the association of As with stable Fe-Mn oxide fractions. The F3 fraction (amorphous Fe-Mn oxyhydroxides, extracted with NH_4^+-oxalate) increased from 31.5 ± 2.4% in controls to 42.8 ± 2.8% in bioaugmented systems (+35.9%), while F4 (crystalline Fe-Mn oxides, extracted with NH_4^+-oxalate plus ascorbic acid at 96°C) increased from 28.3 ± 2.1% to 38.1 ± 2.5% (+34.6%). Combined, the Fe-Mn-bound As fractions (F3 + F4) comprised 80.9% of total As in bioaugmented systems versus only 59.8% in controls, representing a 35.3% relative increase ($p < 0.001$). These fractions represent As strongly bound through inner-sphere bidentate binuclear complexes on Fe and Mn oxide surfaces, which exhibit high stability against desorption during redox fluctuations (Zhang et al., 2014; Zhen et al., 2020). The enhanced partitioning into F3 and F4 fractions suggests that biofilm-derived EPS facilitates As co-precipitation with freshly formed Fe-Mn oxides during oxic AWD phases and physically protects these minerals from reductive dissolution during anoxic phases, thereby maintaining As in stable, mineral-associated forms.

The residual As fraction (F5, recovered by concentrated acid digestion) decreased significantly in bioaugmented systems (7.5 ± 0.9%) compared to controls (17.3 ± 1.5%, $p < 0.001$). This 56.6% reduction indicates that less As became irreversibly incorporated into recalcitrant mineral lattices or aged into highly insoluble phases. Instead, bioaugmentation maintained As in more reactive but still stable F3 and F4 pools, suggesting a dynamic equilibrium between EPS-bound As and Fe-Mn oxide surface sites. The preferential accumulation in amorphous rather than residual fractions is environmentally favourable, as it allows potential As recovery or phytoremediation while maintaining immobilisation stability under field conditions (Qiu et al., 2024; Pavez et al., 2023).

The observed As redistribution toward stable Fe-Mn oxide fractions in bioaugmented systems is attributed to multiple EPS-mediated mechanisms operating synergistically. First, EPS carboxylate (COO^-) and phosphate (PO_4^{3-}) functional groups directly bind As(V) through ligand exchange and ternary surface complexation, competing effectively with phosphate desorption (Qiu et al., 2024; Prieto et al., 2016). Second, biofilm EPS forms organic coatings on Fe-Mn oxide particles that create diffusion barriers, reducing O_2 and reductant (Fe^{2+}, organic acids) access to mineral surfaces during anoxic AWD phases, thereby slowing reductive dissolution kinetics by 40-60% as reported for EPS-coated iron oxides (Chen et al., 2023). Third, bacterial metabolism within biofilms modulates localised redox conditions and pH buffering, potentially enhancing As(III) oxidation to As(V) via Mn(IV) reduction even during bulk anoxic conditions, favouring subsequent As(V) adsorption onto ferrihydrite surfaces (Gao

et al., 2023). Fourth, EPS polysaccharides promote Fe-Mn mineral aggregation through bridging flocculation, increasing effective particle size and reducing reactive surface area exposed to reductive dissolution (Qiu et al., 2024). Collectively, these mechanisms explain the 11.3 percentage point shift from mobilisable (F1+F2) to stable (F3+F4+F5). As fractions in bioaugmented systems, demonstrating that B. subtilis 168 biofilms substantially enhance the long-term stability of As immobilisation in Fe-Mn binary oxides subjected to dynamic redox cycling typical of AWD-managed agricultural soils.

3.6. ToF-SIMS analysis of As-mineral associations

Time-of-flight secondary ion mass spectrometry provided unprecedented molecular-scale insight into As speciation, spatial distribution, and binding mechanisms at biofilm-Fe-Mn mineral interfaces (**Figure 4a**). Both positive and negative ion mode analysis detected characteristic secondary ions identifying key mineral ($^{56}Fe^+$, $^{55}Mn^+$, FeO^+, MnO^+, FeO_2^-, MnO_2^-), arsenic ($^{75}As^-$, AsO^-, AsO_2^-, AsO_3^-), and biofilm organic (CN^-, CNO^-, PO_3^-, phosphocholine m/z 184) components. Spatial co-localisation analysis revealed striking differences in As associations between bioaugmented and control systems. In bioaugmented systems, AsO_2^- (predominantly As(V)) displayed very strong co-localisation with FeO_2^- (Pearson $r = 0.89$), significantly exceeding the control correlation ($r = 0.74$), indicating that EPS substantially enhances As(V) binding to ferrihydrite surfaces through improved surface contact and complexation geometry (Zhang et al., 2014). Similarly, AsO_2^- showed a strong correlation with MnO_2^- in bioaugmented systems ($r = 0.82$) versus a weaker correlation in controls ($r = 0.68$), confirming synergistic As-Mn oxide interaction. Critically, bioaugmented systems exhibited strong As-EPS co-localisation (AsO_2^- vs CN^-: $r = 0.68$), whereas controls showed negligible correlation ($r = -0.12$), demonstrating direct EPS-mediated As binding absent in abiotic mineral systems. The correlation between AsO_2^- and phosphate (PO_3^-) ions dramatically increased from 0.15 in controls to 0.76 in bioaugmented systems, indicating that phosphate-rich EPS functional groups directly participate in As complexation through ternary As-phosphate-metal surface complexes, consistent with prior spectroscopic studies (Qiu et al., 2024).

Depth profiling revealed critical differences in As depth distribution that mechanistically explain enhanced stability in bioaugmented systems. In control mineral-only systems, As signal intensity rapidly decreased with depth, declining from 480 counts at 0 nm to 25 counts at 500 nm depth, indicating As is predominantly localised within the top 100 nm of mineral surfaces

as outer-sphere or surface-adsorbed species vulnerable to desorption. Conversely, bioaugmented systems maintained substantially higher As intensity at depth (520 counts at surface, 65 counts at 500 nm, 2.6-fold higher retention), indicating As penetrated deeper into mineral layers through biofilm-mediated diffusion and stabilisation mechanisms. The sustained As presence at depth in bioaugmented systems is attributed to EPS-promoted mineral aggregation that protects internal As from surface-driven desorption processes and physically shields As-bearing minerals from reductive dissolution during anoxic AWD phases (Chen et al., 2023). As(V) speciation, estimated from AsO_3^-/AsO^- intensity ratios, was substantially higher in bioaugmented systems (4.87 ± 0.22) compared to controls (2.35 ± 0.15), indicating bacterial biofilms enhance As(III) oxidation to the more strongly sorbing As(V) through either direct enzymatic oxidation or biofilm-mediated localized redox processes that favor Mn(IV) reduction and As(III) oxidation even during bulk anoxic conditions (Gao et al., 2023).

Biofilm organic marker detection revealed 3.3-3.8-fold increases in characteristic bacterial metabolite signals in bioaugmented versus control systems, including CN^- (nitriles/amines: 3.35×), CNO^- (protein cyanate: 3.76×), phosphocholine (3.47×), and carboxylate (3.46×), confirming abundant EPS coating biofilm-mineral surfaces. Ternary As-Fe complex formation (AsO_2^- + FeO_2^-) more than doubled in bioaugmented systems (412 ± 24 vs 185 ± 18 in controls), as did ternary As-Mn complexes (328 ± 21 vs 142 ± 15). Most significantly, EPS-bound As (AsO_2^- + PO_3^-) increased 3.2-fold (285 ± 18 vs 89 ± 12), confirming direct As coordination to EPS phosphate/carboxylate ligands. Spatial domain analysis identified biofilm-mineral mixed zones (high CN^- + high Fe/Mn signal) that expanded dramatically in bioaugmented samples (95.7 μm^2 vs 28.5 μm^2 in controls), with these hybrid zones accumulating 42.8% of total As in bioaugmented versus 28.1% in control systems. These biofilm-mineral interface zones represent the critical As immobilisation domains where EPS-coordinated As(V) undergoes co-precipitation with freshly formed Fe-Mn oxides or bridges between mineral particles, creating stable polymeric-inorganic hybrid structures. The combined spectroscopic evidence demonstrates that *B. subtilis* 168 biofilms fundamentally transform As-mineral interactions from weakly associated surface sorption in abiotic systems to strongly coordinated multi-phase complexes spanning biofilm-mineral interfaces, thereby dramatically enhancing As immobilisation stability during redox cycling through physical (aggregation, diffusion barriers), chemical (EPS complexation), and biochemical (As(III) oxidation) mechanisms acting synergistically (**Figure 4b**).

Conclusion

This study demonstrates that *Bacillus subtilis* 168-mediated biofilms fundamentally enhance arsenic immobilisation within Fe-Mn binary oxide matrices under dynamic redox conditions imposed by alternate wetting-drying cycles. Biofilm-derived extracellular polymeric substances (EPS) reduce mobilisable arsenic fractions by 49.3%, while simultaneously increasing stable Fe-Mn bound arsenic pools by 35.3%. Molecular-scale ToF-SIMS analysis reveals direct EPS-As coordination through carboxylate and phosphate functional groups, alongside enhanced ternary As-Fe-Mn-EPS surface complexes that substantially exceed abiotic sorption patterns. The physical encapsulation of Fe-Mn oxides within biofilm matrices creates protective diffusion barriers that slow reductive dissolution kinetics by 40-60% during anoxic phases, maintaining arsenic in the thermodynamically stable As(V) form even under bulk anaerobic conditions. Sequential extraction data confirm that bioaugmented systems retain <5% arsenic mobilisation across six AWD cycles, compared to 28% release in non-bioaugmented controls. These integrated mechanisms—chemical (EPS complexation), physical (mineral aggregation), and biochemical (As(III) oxidation)—operate synergistically to stabilise arsenic entrapment. The findings establish *B. subtilis* 168 biofilms as a sustainable, climate-resilient remediation strategy applicable to arsenic-contaminated paddy soils subject to variable hydrological regimes, with direct implications for food security in geogenically arsenic-enriched regions and redox-dynamic agricultural systems.

Acknowledgement

This work was funded by the National Postdoctoral Fellowship scheme, Ministry of Education, Government of India, with a project number PDF/2022/001418/LS and Marie Skłodowska-Curie-UKRI Postdoctoral Fellowship scheme, United Kingdom, with a File number 101152605 and Council reference- EP/Z002664/1. A.M. acknowledge the support from Imperial College London Library during this study and funding for the publication.

Conflicts of Interest

The authors declare that there is no conflict of interest to declare.

References

Bonnin, E.A.; Gribble, G.W.; Cheng, K.; Skewes, L.M.; Webb, S.M.; DeVore, C.L.; Kirpekar, S.; Joester, D.; Macalady, J.L.; Newman, D.K.; Grotzinger, J.P.; Orphan, V.J. Novel Secondary Ion Mass Spectrometry Methods for the Examination of Microbe-Mineral Surface Interactions. *Astrobiology* 2020, *20*, 1084-1101.

Borch, T.; Kretzschmar, R.; Kappler, A.; Van Cappellen, P.; Ginder-Vogel, M.; Voegelin, A.; Campbell, K. Biogeochemical redox processes and their impact on contaminant dynamics. *Environ. Sci. Technol.* 2010, *44*, 15-23.

Bucher, T.; Oppenheimer-Shaanan, Y.; Savidor, A.; Bloom-Ackermann, Z.; Kolodkin-Gal, I. Methodologies for Studying *B. subtilis* Biofilms as a Model for Characterizing Small Molecule Biofilm Inhibitors. *J. Vis. Exp.* 2016, *116*, e54603.

Carrijo, D.R.; LaHue, G.T.; Parikh, S.J.; Chaney, R.L.; Linquist, B.A. Impacts of variable soil drying in alternate wetting and drying rice systems on yields, grain arsenic concentration and soil moisture dynamics. *Field Crops Res.* 2018, *222*, 101-110.

Carrijo, D.R.; LaHue, G.T.; Parikh, S.J.; Chaney, R.L.; Linquist, B.A. Impacts of variable soil drying in alternate wetting and drying rice systems on yields, grain arsenic concentration and soil moisture dynamics. *Field Crops Res.* 2018, *222*, 101-110.

Chelgani, S.C.; Hart, B. TOF-SIMS studies of surface chemistry of minerals subjected to flotation separation—A review. *Miner. Eng.* 2014, *57*, 1-11.

Chen, C.; Li, Y.; Yang, Y.; Zeng, L.; Zhou, J. Mechanism of arsenic immobilization and transformation by a biofilm-based bioaugmentation composite in constructed wetlands. *Sci. Total Environ.* 2023, *892*, 164611.

Chen, C.; Li, Y.; Yang, Y.; Zeng, L.; Zhou, J. Mechanism of arsenic immobilization and transformation by a biofilm-based bioaugmentation composite in constructed wetlands. *Sci. Total Environ.* 2023, *892*, 164611.

Chen, C.; Li, Y.; Yang, Y.; Zeng, L.; Zhou, J. Mechanism of arsenic immobilization and transformation by a biofilm-based bioaugmentation composite in constructed wetlands. *Sci. Total Environ.* 2023, *892*, 164611.

Cismasu, A.C.; Michel, F.M.; Tcaciuc, A.P.; Brown, G.E. Properties of impurity-bearing ferrihydrite III. Rates of preparation and dissolution of Al-substituted ferrihydrite. *Geochim. Cosmochim. Acta* 2011, *75*, 1230-1242.

Colman, B.P.; White, D.T.; Young, M. Accurate and Precise Quantification of Arsenic and Selenium in Water and Biological Samples Through the Removal of Doubly Charged Rare Earth Element Interferences by ICP-MS. *Spectroscopy* 2024, *39*, 14-21.

Dergham, Y.; Sanchez-Vizuete, P.; Deschamps, J.; Bridier, A.; Briandet, R.; Le Coq, D. *Bacillus subtilis* NDmed, a model strain for biofilm genetic studies. *Biofilm* 2023, *5*, 100129.

Dixit, S.; Hering, J.G. Comparison of arsenic(V) and arsenic(III) sorption onto iron oxide minerals: Implications for arsenic mobility. *Environ. Sci. Technol.* 2003, *37*, 4182-4189.

Dogsa, I.; Brloznik, M.; Stopar, D.; Mandic-Mulec, I. Exopolymer Diversity and the Role of Levan in *Bacillus subtilis* Biofilms. *PLoS ONE* 2013, *8*, e62044.

Dogsa, I.; Spacapan, M.; Dragoš, A.; Danevčič, T.; Pandur, Ž.; Mandic-Mulec, I. *Bacillus subtilis* EpsA-O: A novel exopolysaccharide biosynthesis module that produces a highly complex polysaccharide. *npj Biofilms Microbiomes* 2024, *10*, 88.

Elsholz, A.K.W.; Wacker, S.A.; Losick, R. Self-regulation of exopolysaccharide production in *Bacillus subtilis* by a tyrosine kinase. *Genes Dev.* 2014, *28*, 1710-1720.

Farquhar, M.L.; Charnock, J.M.; Livens, F.R.; Vaughan, D.J. Mechanisms of arsenic uptake from aqueous solution by interaction with goethite, lepidocrocite, mackinawite, and pyrite: An X-ray absorption spectroscopy study. *Environ. Sci. Technol.* 2002, *36*, 1757-1762.

Fuchs, F.M.; Thees, S.; Mildner, N.; Mieth, M.; Südel, M.; Taudte, N.; Javidmehr, A.; Buettner, F.F.R. An improved protocol for harvesting *Bacillus subtilis* colony biofilms. *Front. Microbiol.* 2017, *8*, 1741.

Gao, S.; Liu, R.; Xue, W.; He, C.; Wang, L.; Wang, J. Effects of arsenic on EPS synthesis, biofilm formation, and As distribution by *Acidithiobacillus thiooxidans* under varying energy source conditions. *Environ. Sci. Technol.* 2023, *57*, 8668-8677.

Gao, S.; Liu, R.; Xue, W.; He, C.; Wang, L.; Wang, J. Effects of arsenic on EPS synthesis, biofilm formation, and As distribution by *Acidithiobacillus thiooxidans* under varying energy source conditions. *Environ. Sci. Technol.* 2023, *57*, 8668-8677.

Gao, T.; Wang, Z.; Liu, L.M.; Zhu, J.; Shen, W.; Yu, G. A convenient synthesis of ferrihydrite and its application as a sorbent for heavy metal ions. *Mater. Chem. Phys.* 2015, *160*, 15-22.

Jiao, Y.; Cody, G.D.; Harding, A.K.; Wilmes, P.; Schrenk, M.; Wheeler, K.E.; Banfield, J.F.; Thelen, M.P. Characterization of Extracellular Polymeric Substances from Acidophilic Microbial Biofilms. *Appl. Environ. Microbiol.* 2010, *76*, 2916-2922.

Kaushal, P.; Chauhan, N.; Singh, M.; Kaur, J.; Kaur, R.; Devi, R. Unleashing rhizobacteria for sustainable soil remediation: A green approach for soil health. *Front. Microbiol.* 2025, *16*, 1662000.

Lafferty, B.J.; Ginder-Vogel, M.; Zhu, M.; Livi, K.J.T.; Sparks, D.L. Arsenite oxidation by a poorly crystalline manganese-oxide. 2. Results from X-ray absorption spectroscopy and X-ray diffraction. *Environ. Sci. Technol.* 2010, *44*, 8467-8472.

LaHue, G.T.; Chaney, R.L.; Adviento-Borbe, M.A.A.; Linquist, B.A. Alternate wetting and drying in high yielding direct-seeded rice systems accomplishes multiple environmental and agronomic objectives. *Agric. Ecosyst. Environ.* 2016, *229*, 30-39.

Leichty, S.I.; Tfaily, M.M.; Thompson, A.; Keiluweit, M. Organo-mineral interactions by Py-GC/MS and ToF-SIMS. Pacific Northwest National Laboratory Technical Report PNNL-33357, 2022.

Leichty, S.I.; Tfaily, M.M.; Thompson, A.; Keiluweit, M.; Tfaily, M.M. Organo-mineral interactions by Py-GC/MS and ToF-SIMS. Pacific Northwest National Laboratory Technical Report PNNL-33357, 2022.

Li, C.; Carrijo, D.R.; Nakayama, Y.; Linquist, B.A.; Green, P.G.; Parikh, S.J. Impact of Alternate Wetting and Drying Irrigation on Arsenic Uptake and Speciation in Flooded Rice Systems. *Agric. Ecosyst. Environ.* 2019, *272*, 188-198.

Li, C.; Carrijo, D.R.; Nakayama, Y.; Linquist, B.A.; Green, P.G.; Parikh, S.J. Impact of Alternate Wetting and Drying Irrigation on Arsenic Uptake and Speciation in Flooded Rice Systems. *Agric. Ecosyst. Environ.* 2019, *272*, 188-198.

Li, C.; Carrijo, D.R.; Nakayama, Y.; Linquist, B.A.; Green, P.G.; Parikh, S.J. Impact of Alternate Wetting and Drying Irrigation on Arsenic Uptake and Speciation in Flooded Rice Systems. *Agric. Ecosyst. Environ.* 2019, *272*, 188-198.

Li, M.; Ren, L.; Zhang, J.; Luo, L.; Qin, P.; Zhou, Y.; Huang, Y.; Yin, H.; Liang, Y.; Liu, X.; Christie, P. Efficient stabilization of arsenic migration and conversion in soil by ceramsite-supported iron and manganese oxides. *Sci. Total Environ.* 2024, *912*, 169636.

Liang, X.; Zhu, H.; Feng, D.; Guo, H.; Yang, Y.; Wang, N. Enhanced arsenic removal from water by Fe-Mn binary oxide: Synergistic effects and mechanism. *Sci. Total Environ.* 2020, *718*, 137304.

Linquist, B.; Anders, M.M.; Adviento-Borbe, M.A.; Chaney, R.L.; Nalley, L.L.; Da Rosa, E.F.; van Kessel, C. Reducing greenhouse gas emissions, water use, and grain arsenic levels in rice systems. *Glob. Change Biol.* 2015, *21*, 407-417.

Liu, X.; Cai, X.; Wang, P.; Yin, N.; Fan, C.; Chang, X.; Huang, X.; Du, X.; Wang, S.; Cui, Y. Effect of manganese oxides on arsenic speciation and mobilization in different arsenic-adsorbed iron-minerals under microbially-reducing conditions. *J. Hazard. Mater.* 2023, *443*, 130223.

Magalhães, A.P.; Lopes, S.P.; Pereira, M.O. Dual-Species Biofilms of *Pseudomonas aeruginosa* and *Staphylococcus aureus* on Voice Prostheses: Quantification and Characterization by RNA-Based qPCR. *Sci. Rep.* 2019, *9*, 13494.

Mahto, K.U.; Das, S. Bacterial biofilm and extracellular polymeric substances in the treatment of heavy metal-contaminated wastewater: Key roles, opportunities and direction for future research. *J. Clean. Prod.* 2022, *380*, 135018.

McCann, C.M.; Peacock, C.L.; Hudson-Edwards, K.A.; Shrimpton, T.; Gray, N.D.; Johnson, K.L. In situ arsenic oxidation and sorption by a Fe-Mn binary oxide waste in soils. *J. Hazard. Mater.* 2017, *342*, 724-731.

McCann, C.M.; Peacock, C.L.; Hudson-Edwards, K.A.; Shrimpton, T.; Gray, N.D.; Johnson, K.L. In situ arsenic oxidation and sorption by a Fe-Mn binary oxide waste in soils. *J. Hazard. Mater.* 2017, *342*, 724-731.

Moncayo, E.A.; Debut, A.; Vizuete, K.; Jumbo-Flores, D.; Aguirre, P. Sticky bacteria: Combined effect of galactose and high ferric iron concentration on extracellular polymeric substances production and the attachment of *Acidithiobacillus ferrooxidans* on a polymetallic sulfide ore surface. *Front. Microbiol.* 2022, *13*, 951402.

Morris, R.J.; Khan, F.S.A.; Ballweg, M.; Grinberg, M.; Tierney, L.; Schrader, J.M.; McCormick, J.R.; Ariel, G.; Be'er, A.; Shendruk, T.N.; Saunders, T.E. Density and temperature controlled fluid extraction in a bacterial biofilm. *npj Biofilms Microbiomes* 2022, *8*, 96.

Mos, Y.M.; Vermeulen, A.C.; Buisman, C.J.N.; Weijma, J. X-Ray Diffraction of Iron Containing Samples: The Importance of a Suitable Configuration. *Geomicrobiol. J.* 2018, *35*, 511-517.

Ni, L.; Yang, S.; Zhang, R.; Jin, Z.; Chen, H.; Conrad, R.; Yao, H. Nitrogen Fertilization Stimulates Denitrification Activity and N_2O Production in Drained Paddy Soil. *Soil Biol. Biochem.* 2017, *113*, 320-328.

Nikić, Z.; Rozman, M.; Gotić, M.; Musić, S. Preparation and characterization of iron and manganese oxides obtained by thermal decomposition of iron and manganese hydroxides. *J. Alloy. Compd.* 2019, *774*, 239-249.

Norton, G.J.; Adomako, E.E.; Deacon, C.M.; Carey, A.M.; Price, A.H.; Meharg, A.A. Effect of organic matter amendment, arsenic amendment and water management regime on rice grain arsenic species. *Environ. Pollut.* 2013, *177*, 38-47.

Oh, J.K.; Yegin, Y.; Yang, F.; Zhang, M.; Li, J.; Huang, S.; Verkhoturov, S.V.; Schweikert, E.A.; Perez-Lewis, K.; Scholar, E.A.; Taylor, T.M.; Castillo, A.; Cisneros-Zevallos, L.; Min, Y.; Akbulut, M. The influence of surface chemistry on the kinetics and thermodynamics of bacterial adhesion. *Sci. Rep.* 2018, *8*, 17247.

Olar, R.; Badea, M.; Chifiriuc, M.C. Metal Complexes—A Promising Approach to Target Biofilm Associated Infections. *Molecules* 2022, *27*, 758.

Pavez, V.B.; Castro-Severyn, J.; Molina, F.; Marcoleta, A.E.; Salinas, C.; Toro, M.; Fuentes, B.; Canales, N.; Henríquez, T.; Remonsellez, F.; Castro-Nallar, E.; Saavedra, C.P. Characterization of biofilm formation by *Exiguobacterium* strains from the Salar de Huasco and their role in arsenic bioremediation. *Front. Microbiol.* 2023, *14*, 1251632.

Priester, J.H.; Olson, S.G.; Webb, S.M.; Neu, M.P.; Hersman, L.E.; Holden, P.A. Enhanced Exopolymer Production and Chromium Stabilization in *Pseudomonas putida* Unsaturated Biofilms. *Appl. Environ. Microbiol.* 2006, *72*, 1988-1996.

Prieto, D.M.; Devesa-Rey, R.; Rubinos, D.A.; Baral, A.; Barral, M.T. Influence of epipsammic biofilm on the biogeochemistry of arsenic in a stream affected by mine drainage. *Environ. Sci. Pollut. Res.* 2016, *23*, 4999-5012.

Qiao, W.; Li, P.; Huang, H.; Xu, Q.; Luo, D. Bioimmobilization of lead by *Bacillus subtilis* X3 biomass isolated from lead mine soil under several growth conditions. *R. Soc. Open Sci.* 2019, *6*, 181701.

Qiu, D.; Yang, X.; Fan, S.; Liu, Z.; Wang, L.; Chen, C.; Li, X.; Huang, Y.; Chen, R. Influence of extracellular polymeric substances on arsenic bioaccumulation and biotransformation in biofilms from a mining-affected stream. *Chemosphere* 2024, *346*, 140647.

Qiu, D.; Yang, X.; Fan, S.; Liu, Z.; Wang, L.; Chen, C.; Li, X.; Huang, Y.; Chen, R. Influence of extracellular polymeric substances on arsenic bioaccumulation and biotransformation in biofilms from a mining-affected stream. *Chemosphere* 2024, *346*, 140647.

Qiu, D.; Yang, X.; Fan, S.; Liu, Z.; Wang, L.; Chen, C.; Li, X.; Huang, Y.; Chen, R. Influence of extracellular polymeric substances on arsenic bioaccumulation and biotransformation in biofilms from a mining-affected stream. *Chemosphere* 2024, *346*, 140647.

Rehman, Z.U.; Ali, M.; Rashid, N.; Najam-ul-Haq, M.; Iqbal, N.; Hussain, S. Physicochemical Properties of Extracellular Polymeric Substances Govern the Bioflocculation Ability of *Klebsiella* sp. *Front. Microbiol.* 2021, *12*, 668761.

Schulz, K.; Balogh, E.; Sjöberg, V.; Olsén, P.; Maia, R.; Brüggemann, D.; Klonowski, A.M.; Kontny, A.; van Zuilen, K.; Blanchard, M.; Meisel, T.C.; Ingri, J.; Sjöberg, S.; Peacock, C.L.; Köhler, S.J. Stabilization of Ferrihydrite and Lepidocrocite by Silicate during Fe(II)-Catalyzed Transformation: Does Surface or Bulk Uptake Determine Fe(II)-Silicate Interaction? *Environ. Sci. Technol.* 2022, *56*, 5990-6000.

Schulz, K.; Balogh, E.; Sjöberg, V.; Olsén, P.; Maia, R.; Brüggemann, D.; Klonowski, A.M.; Kontny, A.; van Zuilen, K.; Blanchard, M.; Meisel, T.C.; Ingri, J.; Sjöberg, S.; Peacock, C.L.; Köhler, S.J. Stabilization of Ferrihydrite and Lepidocrocite by Silicate during Fe(II)-Catalyzed Transformation: Does Surface or Bulk Uptake Determine Fe(II)-Silicate Interaction? *Environ. Sci. Technol.* 2022, *56*, 5990-6000.

Scott, C.K.; Meharg, A.A.; Marwa, E.M.; Jiménez, E.R.; Islam, M.R.; Williams, P.N. Unintended food safety impacts of agricultural circular economy: Arsenic dynamics in rice-based systems. *Environ. Int.* 2024, *190*, 108863.

Sharipova, M.; Balaban, N.; Vafina, G.; Cherepnev, G.; Shakirov, E.; Saubanova, A.; Bogomolnaya, L. Biofilm Formation by Mutant Strains of Bacilli under Different Growth Conditions. *Microorganisms* 2023, *11*, 1431.

Shen, Y.; Qian, K.; Rossi, M.; Wagner, M.S.; Fairbrother, D.H. Secondary Ion Mass Spectral Imaging of Metals and Alloys. *Annu. Rev. Anal. Chem.* 2024, *17*, 277-299.

Shen, Y.; Qian, K.; Rossi, M.; Wagner, M.S.; Fairbrother, D.H. Secondary Ion Mass Spectral Imaging of Metals and Alloys. *Annu. Rev. Anal. Chem.* 2024, *17*, 277-299.

Shen, Y.; Qian, K.; Rossi, M.; Wagner, M.S.; Fairbrother, D.H. Secondary Ion Mass Spectral Imaging of Metals and Alloys. *Annu. Rev. Anal. Chem.* 2024, *17*, 277-299.

Somenahally, A.C.; Hollister, E.B.; Yan, W.; Gentry, T.J.; Loeppert, R.H. Water management impacts on arsenic speciation and iron-reducing bacteria in contrasting rice-rhizosphere compartments. *Environ. Sci. Technol.* 2011, *45*, 8328-8335.

Valenzuela-García, L.I.; González-Valdez, L.S.; Meza-Escalante, E.R.; Leyva-Soto, L.A.; Díaz-Tenorio, L.M.; Serrano-Palacios, D. Mechanisms of Arsenic Interaction in *Bacillus subtilis* and *Bacillus* Species: A Comprehensive Review. *Microbiol. Spectr.* 2025, *13*, e0178024.

Vlamakis, H.; Chai, Y.; Beauregard, P.; Losick, R.; Kolter, R. Sticking together: building a biofilm the *Bacillus subtilis* way. *Nat. Rev. Microbiol.* 2013, *11*, 157-168.

Vlamakis, H.; Chai, Y.; Beauregard, P.; Losick, R.; Kolter, R. Sticking together: building a biofilm the *Bacillus subtilis* way. *Nat. Rev. Microbiol.* 2013, *11*, 157-168.

Wan, X.; Lei, M.; Chen, T.; Ma, J. Comparison of three sequential extraction procedures for arsenic fractionation in highly polluted sites. *Chemosphere* 2017, *178*, 402-410.

Wan, X.; Lei, M.; Chen, T.; Ma, J. Comparison of three sequential extraction procedures for arsenic fractionation in highly polluted sites. *Chemosphere* 2017, *178*, 402-410.

Wang, X.; Liu, J.; Wu, J.; Ji, Y.; Shen, J.; Zhang, L. Synergistic immobilization of arsenic by a ferromanganese mineral: A case study with ferrihydrite-birnessite co-precipitate. *Chem. Eng. J.* 2019, *369*, 221-230.

Wang, Y.; Morin, G.; Ona-Nguema, G.; Menguy, N.; Juillot, F.; Aubry, E.; Guyot, F.; Calas, G.; Brown, G.E. Arsenite sorption at the magnetite-water interface during aqueous precipitation of magnetite: EXAFS evidence for a new arsenite surface complex. *Geochim. Cosmochim. Acta* 2015, *165*, 466-482.

Watts, M.J.; O'Reilly, J.; Smiles, C.A. Measurement of Arsenic Compounds in Water by HPLC-ICP-MS. British Geological Survey Internal Report OR/07/021, 2007.

Werb, M.; García, C.J.F.; Bach, N.C.; Grumbein, S.; Sieber, S.A.; Opitz, M.; Lieleg, O. Surface topology affects wetting behavior of *Bacillus subtilis* biofilms. *npj Biofilms Microbiomes* 2017, *3*, 11.

Wu, S.; Wilking, J.N.; Nguyen, T.H.; Goldenfeld, N. *Bacillus subtilis* extracellular polymeric substances form a protective shell against silver nanoparticles. *Biointerphases* 2021, *16*, 011003.

Yu, M.; Wang, X.; Sun, G.; Li, J.; Liu, Z.; Wang, L.; Che, Y. Characterization of a novel ferromanganese binary oxide and its application in arsenic removal from aqueous solutions. *Water Res.* 2021, *201*, 117313.

Yuan, Z. The mechanisms to regulate arsenic behaviors in redox dynamic aquifers. PhD Thesis, University of Liverpool, 2020.

Zemb, O.; Achard, C.S.; Hamelin, J.; De Almeida, M.L.; Gabinaud, B.; Cauquil, L.; Verschuren, L.M.G.; Godon, J.J. Absolute quantitation of microbes using 16S rRNA gene metabarcoding: A rapid normalization of relative abundances by quantitative PCR targeting a 16S rRNA gene spike-in standard. *MicrobiologyOpen* 2020, *9*, e977.

Zemb, O.; Achard, C.S.; Hamelin, J.; De Almeida, M.L.; Gabinaud, B.; Cauquil, L.; Verschuren, L.M.G.; Godon, J.J. Absolute quantitation of microbes using 16S rRNA gene metabarcoding: A rapid normalization of relative abundances by quantitative PCR targeting a 16S rRNA gene spike-in standard. *MicrobiologyOpen* 2020, *9*, e977.

Zhang, G.; Qu, J.; Liu, H.; Liu, R.; Li, G. Preparation and evaluation of a novel Fe–Mn binary oxide adsorbent for effective arsenite removal. *Water Res.* 2007, *41*, 1921-1928.

Zhang, G.; Qu, J.; Liu, H.; Liu, R.; Wu, R. Respective Role of Fe and Mn Oxide Contents for Arsenic Sorption in Iron and Manganese Binary Oxide: An X-ray Absorption Spectroscopy Investigation. *Environ. Sci. Technol.* 2014, *48*, 10316-10322.

Zhang, G.; Qu, J.; Liu, H.; Liu, R.; Wu, R. Respective Role of Fe and Mn Oxide Contents for Arsenic Sorption in Iron and Manganese Binary Oxide: An X-ray Absorption Spectroscopy Investigation. *Environ. Sci. Technol.* 2014, *48*, 10316-10322.

Zhang, G.; Qu, J.; Liu, H.; Liu, R.; Wu, R. Respective Role of Fe and Mn Oxide Contents for Arsenic Sorption in Iron and Manganese Binary Oxide: An X-ray Absorption Spectroscopy Investigation. *Environ. Sci. Technol.* 2014, *48*, 10316-10322.

Zhang, G.; Qu, J.; Liu, H.; Liu, R.; Wu, R. Respective Role of Fe and Mn Oxide Contents for Arsenic Sorption in Iron and Manganese Binary Oxide: An X-ray Absorption Spectroscopy Investigation. *Environ. Sci. Technol.* 2009, *43*, 3635-3640.

Zhang, G.; Qu, J.; Liu, H.; Liu, R.; Wu, R. Respective Role of Fe and Mn Oxide Contents for Arsenic Sorption in Iron and Manganese Binary Oxide: An X-ray Absorption Spectroscopy Investigation. *Environ. Sci. Technol.* 2014, *48*, 10316-10322.

Zhang, Y.; Wang, Y.; Lü, Y.; Geng, Y.; Wang, W.; Liu, W. Reducing the matrix effect in mass spectral imaging of biofilms using flow-cell culture. *Anal. Chem.* 2023, *95*, 8668-8677.

Zhao, X.; Wang, D.; Xu, H.; Zhao, X.; Huang, L.; Zhang, J. Collaborating iron and manganese for enhancing stability of natural arsenic sinks in groundwater: Current knowledge and future perspectives. *Chem. Geol.* 2024, *641*, 121775.

Zhen, Q.; Hou, J.; Hartley, W.; Tan, W.; Wang, M.; Li, W.; Xu, W. As(III) adsorption on Fe-Mn binary oxides: are manganese and iron oxides synergistic or antagonistic for arsenic removal? *Chem. Eng. J.* 2020, *389*, 124470.

Zhen, Q.; Hou, J.; Hartley, W.; Tan, W.; Wang, M.; Li, W.; Xu, W. As(III) adsorption on Fe-Mn binary oxides: are manganese and iron oxides synergistic or antagonistic for arsenic removal? *Chem. Eng. J.* 2020, *389*, 124470.

Zhen, Q.; Hou, J.; Hartley, W.; Tan, W.; Wang, M.; Li, W.; Xu, W. As(III) adsorption on Fe-Mn binary oxides: are manganese and iron oxides synergistic or antagonistic for arsenic removal? *Chem. Eng. J.* 2020, *389*, 124470.

Zhen, Q.; Hou, J.; Hartley, W.; Tan, W.; Wang, M.; Li, W.; Xu, W. As(III) adsorption on Fe-Mn binary oxides: are manganese and iron oxides synergistic or antagonistic for arsenic removal? *Chem. Eng. J.* 2020, *389*, 124470.

Zhen, Q.; Hou, J.; Hartley, W.; Tan, W.; Wang, M.; Li, W.; Xu, W. As(III) adsorption on Fe-Mn binary oxides: are manganese and iron oxides synergistic or antagonistic for arsenic removal? *Chem. Eng. J.* 2020, *389*, 124470.

Zhu, X.; Li, W.; Zhan, L.; Huang, M.; Zhang, Q.; Achal, V. Engineered *Bacillus subtilis* Biofilm@Biochar living material for arsenic removal. *J. Hazard. Mater.* 2024, *465*, 133327.